

6

collisionless shocks

6.1 INTRODUCTION

Shocks occur in a gas or liquid when the speed of their interaction with an obstacle exceeds the velocity of the compressional (sound) wave that would ease the deflection of the flow around that obstacle. This process is both non-linear and dissipative. Thus, the phrase "collisionless shock" is at first sight an oxymoron, given that collisions appear to be a necessary part of the shock process. In an ordinary gas, collisions are an effective way to dissipate energy and bend the flow around the obstacle. In a collisionless plasma, where particles do not collide in the usual sense, kinetic processes and collective forces take the place of the collisions that occur in more familiar shocks. Understanding how this occurs under the wide range of parameters found in space and astrophysical plasmas is an ongoing study, but one whose bases we understand through observation, theory, and numerical models.

Collisionless shocks are important in astrophysical, heliospheric, and planetary settings. They are found throughout the heliosphere, wherever the solar wind flows, from the Sun's surface to the heliopause. As we discussed in Chapter 5, collisionless shocks arise when fast streams in the solar wind overtake slow streams, and also when fast ejections of magnetized plasma called coronal mass ejections move swiftly through the ambient solar wind. They are found as bow shocks, standing in the flow in front of all the planets visited to date. They deflect flows around obstacles, heat the plasma, and alter the properties of the flowing plasma and how it interacts with the obstacles. The physical

processes that take place at these shocks depend on the strength of the shock, as measured by its Mach number, the speed of the shock relative to the speed of the equivalent linear wave and local plasma parameters. Consequently, the downstream properties of the shocked plasma also depend on its Mach number.

6.2 SHOCK BASICS

6.2.1 Waves

As discussed in Chapter 3, there are three propagating waves in the plasma at low frequencies, well below the proton gyro-frequency. The **fast magnetosonic wave** compresses and deflects the plasma around an obstacle. The slow magnetosonic wave ^{stretching? straightens?} strengthens the magnetic field while the mass density drops. This is akin to the stretching of the field line, since when a straight field line gets longer, keeping the same mass content, the field strength will remain the same (in a cold plasma) while the density must drop. In a warm plasma, the thermal energy density of the plasma is positively correlated with the number density, and, when the number density drops, the energy density must too. Hence, in a **slow magnetosonic wave**, the magnetic field and number density are anticorrelated. Of the three propagating waves, slow-mode and fast-mode waves, as their names imply, travel most slowly and most rapidly in a plasma, respectively, at least in the magnetohydrodynamic (MHD) approximation that is generally applicable. Figure 6.1 shows a polar plot of the phase velocity

C. f.
Baumjohann
& Treumann
p 179-180.

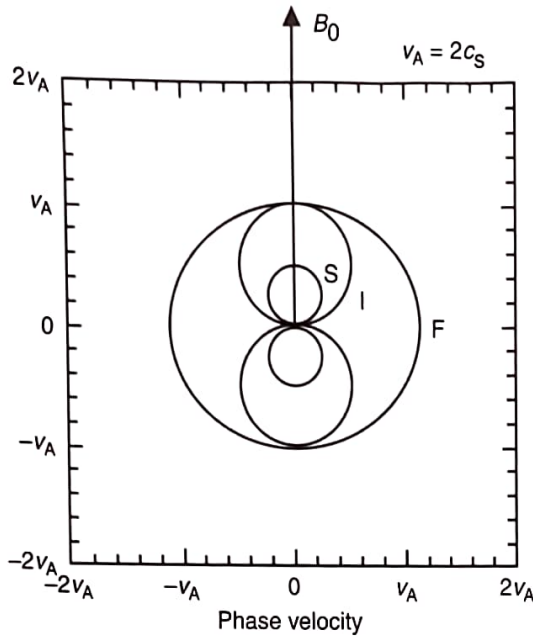


FIGURE 6.1. Polar plot of phase speed of MHD waves in a magnetized plasma in which the Alfvén speed is twice the sound speed. The magnetic field direction is vertical. The fast, intermediate, and slow magnetosonic waves are marked F, I, S, respectively.

of these three modes for the case when the Alfvén speed is twice the sound speed.

The third wave mode in the plasma is the shear Alfvén or intermediate mode, which is a pure bending wave in which the direction of the magnetic field and the plasma velocity change, but the density and magnetic field strength do not. Each of these three waves can be associated with a collisionless shock, but only in a very limited range of circumstances for the intermediate mode. Figure 6.2 shows the variation of density and magnetic field strength versus space or time for the three modes – fast, intermediate, and slow. For the intermediate mode, two orthogonal components of the magnetic field are shown.

6.2.2 Dependence on upstream conditions

Two other factors affect the processes occurring at the shock; the β of the plasma, the ratio of the magnetic to the thermal plasma energy density; and the θ of the magnetic field in the unshocked flow relative to the normal to the shock front. This shock normal angle is usually abbreviated as θ_{B_n} . Because of the latter dependence, the geometry of

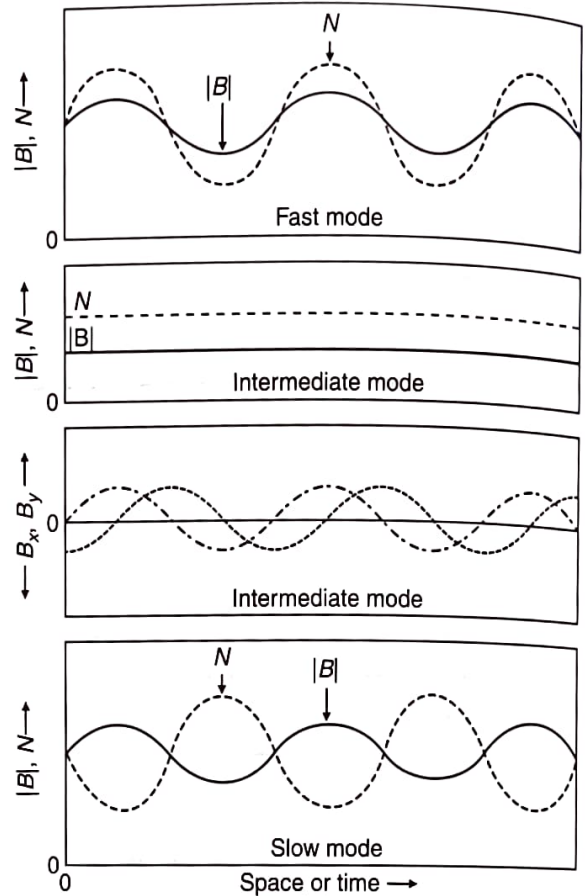


FIGURE 6.2. Waveforms of the fast, intermediate, and slow magnetosonic waves. The signature in the field strength and density are shown for all three waves. Two magnetic components are shown for the intermediate mode because the magnetic field strength and density are constant in this wave.

the interaction is very important, and, since most obstacles to the flowing solar-wind plasma are quasi-spherical objects of different sizes, the radius of curvature of the shock becomes important. Thus, while one-dimensional treatments (as we pursue in this chapter) are instructive, we often have to treat a global model of the interaction in order to understand the observed behavior. We defer discussion of such global models until Chapter 7.

Some of the interest in the study of collisionless shocks stems from their associated acceleration of charged particles to large energies. Systems of collisional particles generally evolve with time to maxwellian distributions with very few particles at high energies. However, in collisionless plasmas, a small minority of the particles can gain a

$$\beta = \frac{p}{B^2/2\mu_0}$$

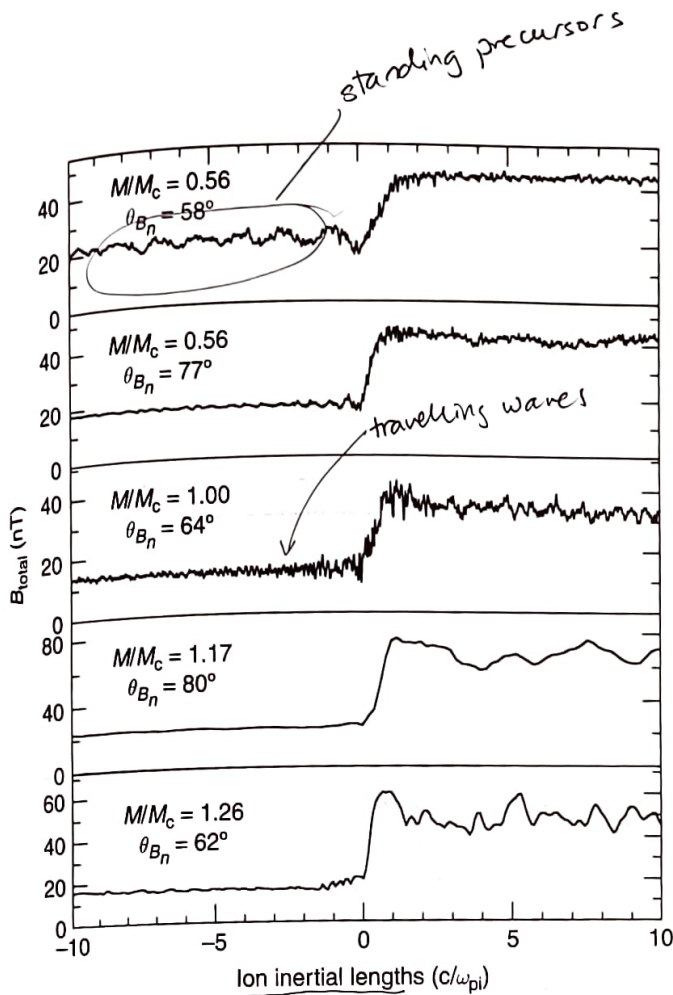


FIGURE 6.3. Observations of magnetic field strength for five shocks of low Mach number, ranging from subcritical to slightly supercritical. All shocks are quasi-perpendicular shocks. The measured temporal profile has been transformed to a distance scale using simultaneous measurements from a companion spacecraft that observed these shocks moments later. The low-frequency upstream waves in the two top panels are standing precursors that move with the shock. The higher-frequency waves are traveling waves in the shock frame. The appearance of these waves is sensitive to the value of θ_{Bn} , the shock normal angle. M_c is the critical Mach number.

$$\rho_i = \frac{U_{1i}}{\Omega_{ci}} = \frac{U_{1i}}{2\pi f_{ci}}$$

$$\text{ion inertial length} \rightarrow d_i = \frac{U_A}{\Omega_{ci}} = \frac{B}{\sqrt{\mu_0 \rho}} \cdot \frac{m_i}{eB} = \sqrt{\frac{m_i^2}{\mu_0 n_i m_i e^2 \epsilon_0}} = \frac{C}{\omega_{pi}}$$

$$\lambda_D = \frac{v_e}{\omega_{pe}}$$

$$\omega_{pi}^2 = \frac{n_i e^2}{m_i \epsilon_0}$$

disproportionate share of the energy, and their distribution of function becomes non-maxwellian. Frequently, the cause of this favoritism of a minority of the particles is acceleration by a collisionless shock. Such acceleration can occur at bow shocks at planetary obstacles, at interplanetary shocks, and at astrophysical shocks in which particles reach ultra-relativistic energies. When these particles enter our solar system, they are called cosmic rays.

Figure 6.3 shows the magnetic field strength during five crossings of the bow shock by ISEE 1 and 2 under a variety of solar-wind conditions, albeit all at low beta and low Mach numbers when the magnetic field was at a large angle to the shock normal. As can be seen, the shock is thin, comparable to, or less than an ion inertial length, the speed of light divided by the ion plasma frequency. When the Mach number is high, or when the magnetic field upstream is more aligned with the shock normal, the fluctuation amplitudes are much greater. We return to the observed structure of the bow shock after we examine the

Rankine-Hugoniot equations that allow us to calculate the change in the average parameters across the shock front. The derivation of these equations from conservation laws and Maxwell's equations is straightforward but lengthy. Since it is important enough and its results used frequently, we include the derivation below. If the reader is only interested in the results, please just skip forward to Eqs. (6.25) and (6.26) near the end of Section 6.3. However, to work with shocks and to use these equations, we must first know how to find the direction of the normal to the shock. This is given in Section 6.2.

6.2.3 The shock normal

As discussed in Section 6.2.2, the angle between the upstream magnetic field and the normal to the shock is one of the most important parameters in determining the nature of the physical processes occurring at the shock. Whereas determination of the orientation of the upstream magnetic field is usually straightforward, determining the orientation of the shock surface may not be

C.F. Baumjohann & Treumann: "A magnetized shock always manages to be locally quasi-perp, even if para. far from the magnetic field"
p. 184

so simple. If the shock is standing in front of a relatively hard obstacle, the shock orientation may be obtained from the known geometry at the interaction. If the shock is oscillating, or if it is a propagating shock, this surface will not be geometrically constrained in any obvious manner. In such a case, we must use other methods to determine the shock surface.

An example of such a constraint is provided by the relative timing and separation of multiple observations of the same planar shock surface. If δx_i ($i = 1, 2, 3, \dots$) are the spatial separations between observations of a shock relative to a spacecraft at x_0 , and if δt_i are the time delays from t_0 , the time of the observation at x_0 , then

4 unknowns
(\hat{n} and $|v|$)

$$\delta x_i \cdot \hat{n} = v \delta t_i, \quad (6.1)$$

where \hat{n} is a unit vector in the direction of the normal to the surface and v is its speed along the normal. If there are more than four observations (i.e., there are more than three baselines), then the equations are over-determined and can be solved by multiplying each side of the equations by the transpose of the δx matrix and inverting to solve for \hat{n} and v . However, we often count ourselves lucky to obtain measurements of a shock with one spacecraft, let alone four.

B connects
with $E \times B$
velocity.

The rate of transport of magnetic flux toward the shock is the tangential component of the electric field. Since magnetic flux does not pile up in the shock layer, our intuition, consistent with Maxwell's equations, tells us that the tangential component of the electric field is conserved across the shock. This, in turn, tells us that the upstream and downstream magnetic field and the shock normal must be coplanar. Thus, the cross product of the upstream and downstream magnetic fields should be perpendicular to the shock normal:

$$(\mathbf{B}_u \times \mathbf{B}_d) \cdot \hat{n} = 0. \quad (6.2)$$

Because the magnetic field is divergenceless,

$$(\mathbf{B}_u - \mathbf{B}_d) \cdot \hat{n} = 0. \quad (6.3)$$

With two different vectors perpendicular to the shock normal, we can calculate a vector along the normal and normalize by the magnitude of the cross product:

$$\hat{n} = (\mathbf{B}_u \times \mathbf{B}_d) \times (\mathbf{B}_u - \mathbf{B}_d) / |(\mathbf{B}_u \times \mathbf{B}_d) \times (\mathbf{B}_u - \mathbf{B}_d)|. \quad (6.4)$$

This direction, of course, is ill defined when $\mathbf{B}_u \parallel \mathbf{B}_d$, which occurs for parallel and perpendicular shocks, both of which are rare in practice. The normal derived in this way is called the coplanarity normal, and the theorem upon which it is based is called the coplanarity theorem. It is a very useful single-spacecraft technique for deriving the shock normal, in part because the magnetic field is generally well calibrated and accurate. The variation of some parameters, such as density, may not even be relatively accurate, let alone absolutely accurate, because their calibration can change across the shock as the temperature varies.

Some researchers use the minimum variance as the shock normal, but this would be true only in situations in which all waves were propagating parallel to the shock normal. This only occurs for some waves in a limited region of parameter space, and we recommend not using this technique for studying the shock jump.

Another constraint that can be used when three-dimensional velocity measurements are available is that

$$(\mathbf{B}_u \times \Delta \mathbf{v}) \cdot \hat{n} = 0 \quad (6.5)$$

and

$$(\mathbf{B}_d \times \Delta \mathbf{v}) \cdot \hat{n} = 0, \quad (6.6)$$

where $\Delta \mathbf{v}$ is the change in the flow velocity from upstream to downstream. When a velocity constraint such as this is combined with a magnetic constraint such as $\Delta \mathbf{B} \cdot \hat{n} = 0$, the resulting normal is called a mixed-mode shock normal. In fact, all these constraints can be combined into one over-determined solution and solved for a best-fit shock normal (Russell *et al.*, 1983). The paper seems to be for interplanetary shocks.

Finally, we note that, with knowledge of the shock normal \hat{n} and use of the continuity equation, we can determine the velocity of the shock relative to the measurement frame. It is possible to show that the shock velocity v_{sh} is

$$v_{sh} = (\rho_d - \rho_u)^{-1} (\rho_d u_d - \rho_u u_u) \cdot \hat{n}, \quad (6.7)$$

where u_d and u_u are the downstream and upstream solar-wind velocities, respectively.

Not the deHoffman-Teller velocity?

$$\nabla \times \mathbf{E} = -\frac{\partial \mathbf{B}}{\partial t}$$

see
Fig 6.19

Once the shock velocity is known, it is possible to convert the time series of a shock observation into a spatial profile by converting time into an appropriate distance unit such as ion inertial length (Figure 6.3) or ion gyro-radii.

Now that we know how to find the shock normal, we can proceed to derive the Rankine-Hugoniot equations that are derived in the normal incidence frame, where the flow is along the shock normal.

6.3 RANKINE-HUGONIOT EQUATIONS

With the establishment of a shock normal coordinate system, we can now express the Rankine-Hugoniot conservation relations in terms of the measured values of the plasma. The Rankine-Hugoniot equations allow us to calculate the downstream state from the upstream state as a function of the strength of the shock, as given by its Mach number. For a fast magnetosonic shock, this is the speed of the shock front, relative to the plasma measured along the shock normal, divided by the speed of the fast magnetosonic wave in the direction of the shock normal in the upstream region. This treatment does not tell us how heating and dissipation occur, only that so much dissipation must occur. One of the assumptions of this treatment is that the spatial changes of the plasma properties are exclusively along the shock normal. The equations are expressed in the normal incidence frame, where the upstream velocity is along the shock normal. Therefore, we assume the gradient is defined as

$$\nabla \equiv \frac{\partial}{\partial n}. \quad (6.8)$$

The Rankine-Hugoniot equations use the conservation equations and Maxwell's equations to derive a set of equations that depend on the upstream state of the plasma (magnetic field strength and orientation, plasma density temperature and velocity) to determine the same parameters downstream as a function of shock strength. We start with an expression for the mass continuity equation. Using our expression for the gradient $\nabla \cdot (\rho u) = 0$, the continuity equation becomes $\partial(\rho u)/\partial n = 0$. If we integrate over n , we can express the above relation as

$$[\rho u_n] = 0, \quad (6.9)$$

where again the bracketed notation indicates the change across the shock boundary. This indicates that the change in mass flux across the shock remains constant. (Change is zero)

For the momentum equation

$$\rho \mathbf{u} \cdot \nabla \mathbf{u} = \nabla P + \mathbf{j} \times \mathbf{B},$$

we get two conservation equations, one for the normal momentum and another for the tangential momentum. For the normal momentum equation, we take only those components which lie along the n direction. Similarly, the tangential momentum equation uses only those components which lie along the l direction, where l is in the plane of the shock along the projection of the upstream magnetic field. Therefore, we obtain for the two equations:

$$\left[\rho u_n + P + \frac{B_l^2}{2\mu_0} \right] = 0, \quad (6.10)$$

$$\left[\rho u_n u_l - \frac{B_n B_l}{\mu_0} \right] = 0. \quad (6.11)$$

The energy equation

$$\nabla \cdot \left[u \left(\frac{\gamma}{\gamma - 1} P + 1/2 \rho u^2 \right) \right] = \mathbf{j} \times \mathbf{E}$$

can be reduced to

$$\left[u_n \left(\frac{\gamma}{\gamma - 1} P + 1/2 \rho u^2 + \frac{B_l^2}{\mu_0} \right) - \frac{u_l B_n B_l}{\mu_0} \right] = 0 \quad (6.12)$$

by using the fact that

$$\mathbf{j} \cdot \mathbf{E} = \mu^{-1} \cdot (\nabla \times \mathbf{B}) \cdot (\mathbf{u} \times \mathbf{B})$$

and providing the proper velocity and magnetic field components. The equation $\nabla \cdot \mathbf{E} = 0$ becomes a tautology ($0 = 0$) when the gradient is taken. Therefore, this equation does not play an important role in obtaining a solution. The equations $\nabla \cdot \mathbf{B} = 0$ and $\nabla \times \mathbf{E} = 0$ become

$$[B_n] = 0, \quad (6.13)$$

$$[u_n B_l - u_l B_n] = 0. \quad (6.14)$$

Therefore, we now have a closed set of equations which can be combined and solved to obtain a solution that we can use to predict the downstream state. To achieve our goal of expressing the downstream state, indicated by subscript 2, in terms of the upstream state, indicated by subscript 1, we rewrite the above equations as follows:

$$\rho_1 u_{1n} = \rho_2 u_{2n}, \quad (6.9a)$$

$$\begin{aligned} \rho_1 u_{1n}^2 + \rho_1 K T_1 / m + B_{1l}^2 / 2\mu_0 \\ = \rho_2 u_{2n}^2 + \rho_2 K T_2 / m + B_{2l}^2 / 2\mu_0, \end{aligned} \quad (6.10a)$$

$$B_{1n} B_{1l} / \mu_0 = B_{2n} B_{2l} / \mu_0 - \rho_2 u_{2n} u_{2l}, \quad (6.11a)$$

$$\begin{aligned} u_{1n} \left(\gamma(\gamma - 1)^{-1} \rho_1 K T_1 / m + 0.5 \rho_1 u_{1n}^2 + B_{1l}^2 / \mu_0 \right) \\ = u_{2n} \left(\gamma(\gamma - 1)^{-1} \rho_2 K T_2 / m + 0.5 \rho_2 u_{2n}^2 + 0.5 \rho_2 u_{2l}^2 \right. \\ \left. + B_{2l}^2 / \mu_0 \right) - u_{2l} B_{2n} B_{2l} / \mu_0, \end{aligned} \quad (6.12a)$$

$$B_{1n} = B_{2n}, \quad (6.13a)$$

$$u_{1n} B_{1l} = u_{2n} B_{2l} - u_{2l} B_{2n}, \quad (6.14a)$$

and define dimensionless parameters

$$\begin{aligned} x &= \rho_2 / \rho_1, \quad y = u_{2n} / u_{1n}, \quad z = u_{2l} / u_{1n}, \\ w_1 &= (k T_1 / m u_{1n}^2)^{1/2}, \quad w_2 = (k T_2 / m u_{1n}^2)^{1/2}, \\ b_n &= B_n (\mu_0 \rho_1 u_{1n}^2)^{-1/2}, \quad b_{1l} = B_{1l} (\mu_0 \rho_1 u_{1n}^2)^{-1/2}, \\ b_{2l} &= B_{2l} (\mu_0 \rho_1 u_{1n}^2)^{-1/2} \end{aligned}$$

Using these definitions, our Rankine-Hugoniot equations become

$$1 = xy, \quad (6.9b)$$

$$2(w_1^2 + 1) + b_{1l}^2 = 2x(w_2^2 + y^2) + b_{2l}^2, \quad (6.10b)$$

$$b_n b_{1l} = b_n b_{2l} - xyz, \quad (6.11b)$$

$$\begin{aligned} 2(b_{1l}^2 + \gamma(\gamma - 1)^{-1} w_1^2) + 1 \\ = \gamma(y^2 + z^2 + 2b_{2l}^2 - 2b_n b_{2l} + 2\gamma(\gamma - 1)^{-1} x w_2^2), \end{aligned} \quad (6.12b)$$

and

$$b_{1l} = y b_{2l} - z b_n. \quad (6.14b)$$

The relationship in the first equation can be used to remove x from the following three, and, using the third and fifth equations, we can solve for b_{2l} and z , obtaining

$$\begin{aligned} b_{2l} &= b_{1l} (b_n^2 - 1) (b_n^2 - y)^{-1}, \\ z &= b_{1l} b_n (y - 1) (b_n^2 - y)^{-1}. \end{aligned}$$

Continuing this procedure, we obtain a fourth-order equation in y . To keep better track of the coefficients for the quartic equation, we introduce four variables, which can be expressed in terms of the original measured parameters, as well as those variables defined above. The four defined variables are

$$\begin{aligned} a &\equiv w_1^2 \equiv K T_1 / (m u_{1n}^2), & b &\equiv b_n^2 \equiv B_n^2 / (\mu_0 \rho_1 u_{1n}^2), \\ c &\equiv b_{1l}^2 \equiv B_{1l}^2 / (\mu_0 \rho_1 u_{1n}^2), & d &\equiv \gamma(\gamma - 1)^{-1}. \end{aligned}$$

With these defined variables, the quartic equation in y is given by

$$\begin{aligned} y^4 (1 - 2d) + y^3 (2d + 2ad + cd + 4bd - 2b) \\ + y^2 (b^2 + bc - 4bd - 4abd - 2bcd - 2b^2 d - 2c \\ - 2ad - 1) + y (2b^2 d + 2ab^2 d + 2bcd + 4abd \\ + 2b - cd) + (2c - bc - b^2 - 2ab^2 d) = 0. \end{aligned} \quad (6.15)$$

We can reduce this equation to a cubic equation in y by noting that this equation has one trivial root, $y = 1$, corresponding to no shock at all. The cubic equation becomes

$$y^3 + py^2 + qy + r = 0,$$

where

$$\begin{aligned} p &= [d(2a + c + 4b) - 2b + 1] / (1 - 2d), \\ q &= [-d(4ab + 2bc + 2b^2 - c) + bc - 2c \\ &\quad + b^2 - 2b] / (1 - 2d), \end{aligned}$$

and

$$r = b(2abd + b + c) / (1 - 2d).$$

Depending on the coefficients p , q , and r in the cubic equation, there will be at least one and as many as three real roots. If we define

$$Q \equiv (p^2 - 3q)/9, \quad R \equiv (2p^3 - 9pq + 27r)/54,$$

and the expression $Q^3 - R^2 \geq 0$, there are three real roots, which are

$$y = -2Q^{1/2} \cos((\varphi + n\pi)/3) - p/3, \text{ for } n = 0, 2, 4, \quad (6.16)$$

where

$$\varphi = \cos^{-1}(R/Q^{3/2}).$$

If the expression $Q^3 - R^2 < 0$, there is one real root, which is

$$y = R/|R| \left[(R^2 - Q^3 + |R|)^{1/3} + Q \{ (R^2 - Q^3)^{1/2} + |R| \}^{-1/3} \right] - (p/3). \quad (6.16a)$$

It is important to note that, although there may be three real roots, the root for which $n = 2$ is the only physically interesting root for our discussion of planetary bow shocks. Therefore, depending on the sign of the expression $Q^3 - R^2$, we use either Eq. (6.16a) or Eq. (6.16) with $n = 2$ to determine the parameters for the subsonic downstream state.

We can now calculate the downstream state of the plasma from the upstream parameters. Since parameter y is defined to be the ratio between the downstream and upstream velocities along the shock normal,

$$u_{2n} = y u_{1n}. \quad (6.17)$$

The ratio between the downstream and upstream densities is the reciprocal of the above relation, thus

$$\rho_2 = \rho_1 / y. \quad (6.18)$$

Using the definitions for x , y , z , etc. and Eq. (6.16), we can obtain additional downstream values of the plasma:

$$u_{2l} = u_{1n}(y-1)(bc)^{1/2}(b-y)^{-1} \quad (6.19)$$

and

$$B_{2l} = (\mu_0 \rho_1 u_{1n}^2 c \delta)^{1/2}, \quad (6.20)$$

where

$$KT_2 = m u_{1n}^2 y \left(a + (1-\delta)c/2 - y + 1 \right), \quad (6.21)$$

$$\delta = (b-1)^2(b-y)^{-2}.$$

The parameter δ is the square of the tangential component of the magnetic field. From these expressions in Eqs. (6.19)–(6.21), we can calculate the magnitude of the velocity and magnetic field downstream by

$$\begin{aligned} |u_2| &= (u_{2n}^2 + u_{2l}^2)^{1/2} \\ &= u_{1n}(y^2 + bc(y-1)^2(b-y)^{-2})^{1/2} \end{aligned} \quad (6.22)$$

and

$$|B_2| = (B_{2n}^2 + B_{2l}^2)^{1/2} = (\mu_0 \rho_1 u_{1n}^2 (b + c\delta))^{1/2}. \quad (6.23)$$

A note should be made about comparing predicted values of the downstream plasma using the above relations with measured values from spacecraft. It is very easy to compare directly the densities, temperatures, and magnetic field strengths measured by spacecraft with the Rankine-Hugoniot predicted values because the absolute values of these parameters are not frame dependent. However, we must remember that certain assumptions were made previously about the direction of the flow across the shock. It is important to remember that a frame transformation was executed so that the direction of the upstream plasma flow is aligned along the shock normal. This fact means that there may be a residual velocity component in the \mathbf{m} direction along the shock front for the measured velocity not taken into account for the predicted velocity. Therefore, care must be taken when comparing measured and predicted velocities due to the use of a special coordinate system.

We note that this frame is different from the de Hoffman-Teller frame, in which the frame travels along the shock at a speed sufficient to align the flow along the magnetic field (rather than the normal, as shown here). Hence, there is no motional electric field in the de Hoffman-Teller frame. The velocity of the frame is $v_{HT} = \hat{n} \times (\bar{\mathbf{u}}_u \times \mathbf{B}_u) / (\hat{n} \cdot \mathbf{B}_u)$. Since the normal component of \mathbf{B} and the transverse component of $\mathbf{u} \times \mathbf{B}$ are conserved across the

$\rho \cdot 2 \cdot 02$

$\bar{\mathbf{u}}_u \parallel \hat{n}$ (see p. 203)

shock, the de Hoffman–Teller velocity is the same on both sides of the shock. In this frame, particles simply spiral around the magnetic field line and move along it. Furthermore, since \mathbf{E} is zero, the energies of particles are constant in this frame.

It is also possible to describe the plasma with four dimensionless upstream parameters: plasma beta, β , the fast magnetosonic Mach number, M_{ms1} , the angle of the upstream field to the shock normal, $\theta_{B_{1n}}$, and the ratio of specific heats, γ .

Doing this, we obtain for the upstream version of the four parameters

$$\begin{aligned}\beta_1 &= 2a/(b+c); \theta_{B_{1n}} = \cos^{-1}(b/(b+c))^{1/2}; \\ \gamma &= d/(d-1); \\ M_{ms1} &= (0.5(b+c+ad)/(d-1) \\ &\quad + ((b+c+ad/(d-1))^2 - 4abd/(d-1))^{1/2})^{-1/2},\end{aligned}\quad (6.24)$$

where

$$\begin{aligned}a &= \beta_1/(M_{ms1}^2 K_0); \quad b = 2\cos^2\theta_{B_{1n}}/(M_{ms1}^2 K_0); \\ c &= 2\sin^2\theta_{B_{1n}}/(M_{ms1}^2 K_0); \quad d = \gamma(\gamma-1);\end{aligned}$$

and

$$\begin{aligned}K_0 &= 1 + \gamma\beta_1/2 + (1 + \gamma^2\beta_1^2/4 + \gamma\beta_1 \\ &\quad \times (1 - 2\cos^2\theta_{B_{1n}}))^{1/2}.\end{aligned}$$

With these expressions for a , b , c , and d , we can obtain γ and the parameters for the downstream state.

Since upstream plasma can be fully described by four dimensionless parameters, the same is true for the downstream plasma. Using our definitions of these dimensionless parameters and the expressions for the downstream values of the plasma given, expressions for the dimensionless parameters downstream can be derived. They become

$$\begin{aligned}\beta_2 &= 2(a + 0.5c(1-\delta) + 1 - \gamma)/(b + c\delta); \\ \theta_{B_{2n}} &= \cos^{-1}(b/(b + c\delta))^{1/2}; \\ M_{ms2} &= 2(\gamma^2 + bc(\gamma-1)^2/(b-\gamma)^2)/[\gamma(b + c\delta) \\ &\quad \times (1 + 0.5\gamma\beta_2 + (1 + \gamma^2\beta_2^2/4 + \gamma\beta_2 \\ &\quad \times (1 - 2\cos^2\theta_{B_{2n}}))^{1/2})],\end{aligned}\quad (6.25)$$

where the ratio of specific heats γ is assumed to remain constant through the shock.

As the shock is crossed, the beta (in most cases) will go up, the angle $\theta_{B_{2n}}$ will increase toward 90° , and the Mach number will be below unity. The jumps in the magnetic field strength, density, temperature, and the plasma beta across the shock can be determined using what we have derived in the preceding paragraphs,

$$\begin{aligned}\rho_2/\rho_1 &= \gamma^{-1}; \\ |B_2|/|B_1| &= (\cos^2\theta_{B_{1n}} + \delta\sin^2\theta_{B_{1n}})^{1/2} \\ &= [(b + c\delta)/(b + c)]^{1/2}; \\ \beta_2/\beta_1 &= a^{-1}(b + c)(a + 0.5c(1-\delta) + 1 - \gamma) \\ &\quad \times (b + c\delta)^{-1}; \\ T_2/T_1 &= a^{-1}\gamma(a + 0.5c(1-\delta) + 1 - \gamma).\end{aligned}\quad (6.26)$$

With the equations in Eq. (6.24), we are now equipped to determine how parameters change across the shock as a function of Mach number, beta, and $\theta_{B_{1n}}$. Figure 6.4 compares contour plots of the jump in density and the jump in magnetic field strength as a function of upstream $\theta_{B_{1n}}$ and Mach number for three different betas. At a $\theta_{B_{1n}}$ of 90° , the jump in density and magnetic field are the same, asymptoting to 4 (for a γ of $5/3$) at high Mach number. For parallel shocks with $\theta_{B_{1n}}$ of 0° , the jump is very different for the density and magnetic field. Generally, the density is less sensitive to changing $\theta_{B_{1n}}$ than the magnetic field strength. At a beta of zero, the low Mach number behavior is complicated by the phenomenon known as a switch-on shock, which we discuss in Section 6.4.

Figure 6.5 compares contour plots of the jump in the tangential component of B and in the temperature across the shock as a function of $\theta_{B_{1n}}$ and Mach number. Examining first the plots for high beta, we see that, independent of $\theta_{B_{1n}}$, these jumps increase monotonically as the Mach number increases.

For lower beta, the behavior changes markedly for the tangential component, and slightly for temperature. We see a slight change of the jump in temperature for changing $\theta_{B_{1n}}$ for both $\beta = 0$ and $\beta = 1$, albeit in opposite senses. For the tangential component of B , there is a very marked change in the $\theta_{B_{1n}}$ dependence. At $\theta_{B_{1n}} = 90^\circ$, there is a monotonic increase at $\beta = 0$ and $\beta = 1$, very similar to $\beta \rightarrow \infty$. However, near $\theta_{B_{1n}} = 0^\circ$, the values increase

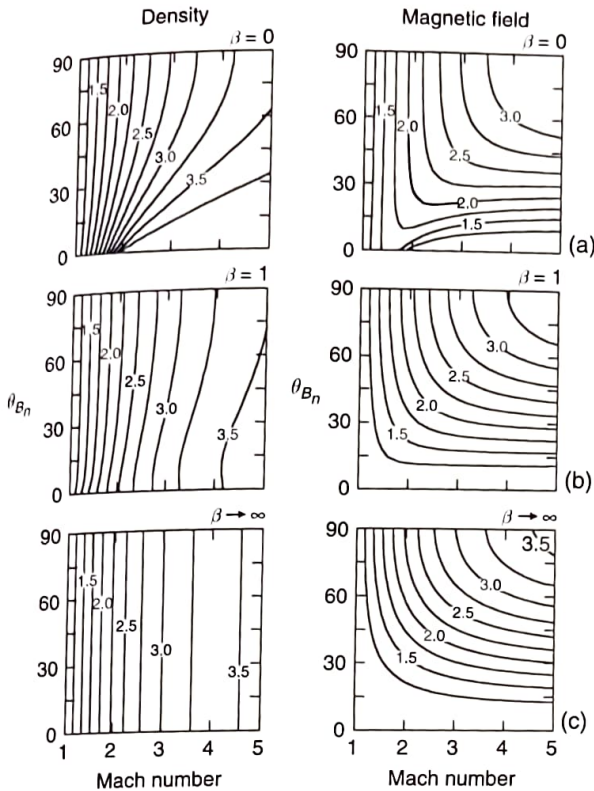


FIGURE 6.4. Contour plots of the jump in density and magnetic field strength as a function of the angle of the upstream magnetic field direction to the shock normal, θ_{B_n} , and the magnetosonic Mach number derived from the Rankine-Hugoniot equations. Contours for (a) $\beta = 0$; (b) $\beta = 1$; (c) $\beta \rightarrow \infty$.

and then decrease with increasing Mach number. This is related to the switch-on shock. This behavior is almost counter-intuitive.

Figure 6.6 compares contour plots of the jump in downstream beta and downstream Mach number as a function of θ_{B_n} and upstream magnetosonic Mach number. The downstream Mach number has the simplest behavior. It monotonically decreases with increasing upstream Mach number with almost no θ_{B_n} dependence at high beta, weak dependence for $\beta = 1$, and stronger dependence at $\beta = 0$. The behavior of downstream beta is quite interesting. At $\beta \rightarrow 0$, the downstream beta at low Mach number drops across the shock. Eventually it increases. At $\beta = 1$, low Mach number, nearly perpendicular shocks have a drop in beta but then an increase at higher Mach number. At high beta,

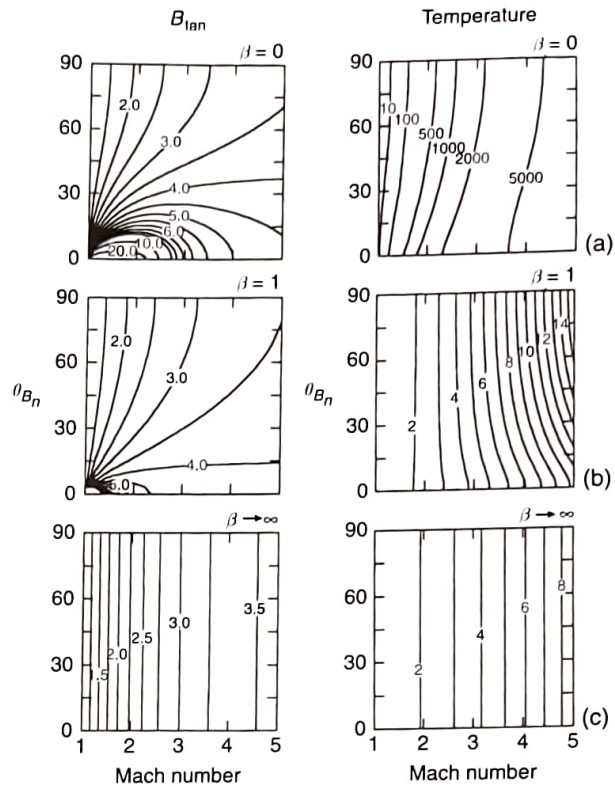


FIGURE 6.5. Contour plots of the jump in B_{tan} and the temperature. Comments of Figure 6.4 apply. Contours for (a) $\beta = 0$; (b) $\beta = 1$; (c) $\beta \rightarrow \infty$.

there is an increase in beta across the shock at all angles and Mach numbers.

✎

6.4 OBSERVATIONS OF PARALLEL AND PERPENDICULAR SHOCKS

The generalized MHD Rankine-Hugoniot equations are very powerful as they allow us to predict the downstream state from the upstream state for any conceivable solar-wind condition as long as the MHD approximations hold. However, they tell us nothing about how the dissipation needed by the shock occurs. To understand this dissipation, we must explore the kinetic processes at the shock. For this purpose, high-resolution magnetic field measurements prove to be instructive. Before we explore that territory more generally, it is helpful to examine the behavior of the shock in two end-member states. We look at the nearly parallel

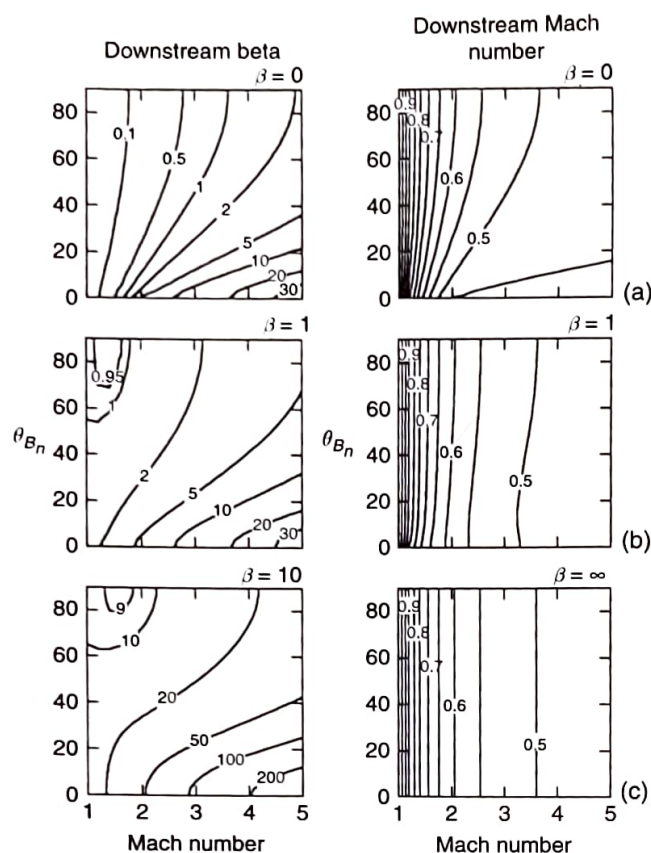


FIGURE 6.6. Contour plots of downstream beta and downstream Mach number. Contours for (a) $\beta = 0$; (b) $\beta = 1$; (c) $\beta \rightarrow \infty$.

shock and its manifestation in the laminar switch-on shock, as well as at the nearly perpendicular shock. Laminar shocks occur when both the Mach number and beta are low, e.g., less than 2 and 0.5, respectively. In the solar wind, shocks are often weak, but the beta is seldom small. The most promising place to find laminar shocks is at the inner planets, where there is always a shock and occasionally the IMF is very large, causing both the Mach number and the beta to drop into the laminar range together.

6.4.1 Parallel laminar shocks

Parallel shocks are very rare because the probability that two uncorrelated vectors will be aligned is very low, much lower than them being orthogonal, for which there are an infinite number of directions. The Rankine-Hugoniot relations tell us that, in general, a parallel shock should produce a jump in

density and temperature, but, because the divergence of the magnetic field is zero, there should be no magnetic field jump. At low Mach numbers, which are rare at the Earth's bow shock, we might expect upstream waves, radiating along the shock normal. These would damp slowly as they would be propagating parallel to the field as well as parallel to the shock normal. There is a surprise, however, illustrated in the top left-hand panel of Figure 6.5. For laminar shocks, at low beta and low Mach numbers, there is a large jump in the tangential component of the magnetic field for nearly parallel shocks. This phenomenon is called the switch-on shock. Figure 6.7 shows the magnetic field in shock normal coordinates for a laminar nearly parallel shock (Farris *et al.*, 1994). The average upstream magnetic field is zero in the two tangential components with the magnetic field lying along the shock normal. The upstream wave train, on the right, shows little damping. Behind the shock, on the left, the field suddenly jumps to 20 nT. Figure 6.8 shows the plasma (electron) moments. The density increases at the field increase as the plasma flows through the shock, the velocity drops, and the temperature rises. We note that, even under laminar shock conditions, the quasi-parallel and parallel shocks are quite unsteady.

6.4.2 Perpendicular shocks

The magnetic profiles of strong quasi-perpendicular shocks consist of a turbulent foot, a jump in field across a ramp region followed by an overshoot, and an undershoot in the magnetic field strength. These features are determined by ion dynamics. The foot length is produced by the turn around of specularly reflected ions at the shock and can be used to determine how fast the shock is moving when there is only a single-spacecraft observation. So, too, the thickness of the ramp and overshoot are associated with ion dynamics, with the ramp thickness being about 0.4 ion inertial lengths. Furthermore, simulations of quasi-perpendicular shocks reproduce the shock structure and the ion dynamics quite well.

For perpendicular shocks, finite ion inertia is not expected to play a role in the dispersive structure of the shock. Rather, the shock thickness is expected to be of the order of the electron inertial length,

perfectly perp.?

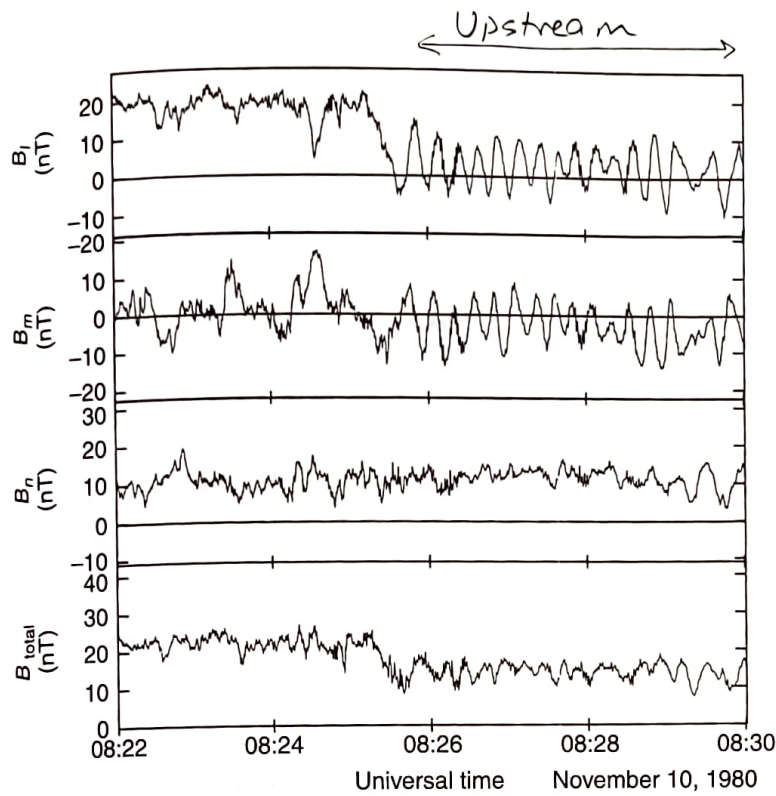


FIGURE 6.7. Magnetic field measurements across a switch-on shock in shock normal coordinates. The n -direction is along the shock normal, the l -direction is parallel to the downstream component of the magnetic field in the shock plane. Mach number = 1.14 ± 0.7 ; $\beta = 0.2$, and $\theta_{B_n} = 17^\circ$.

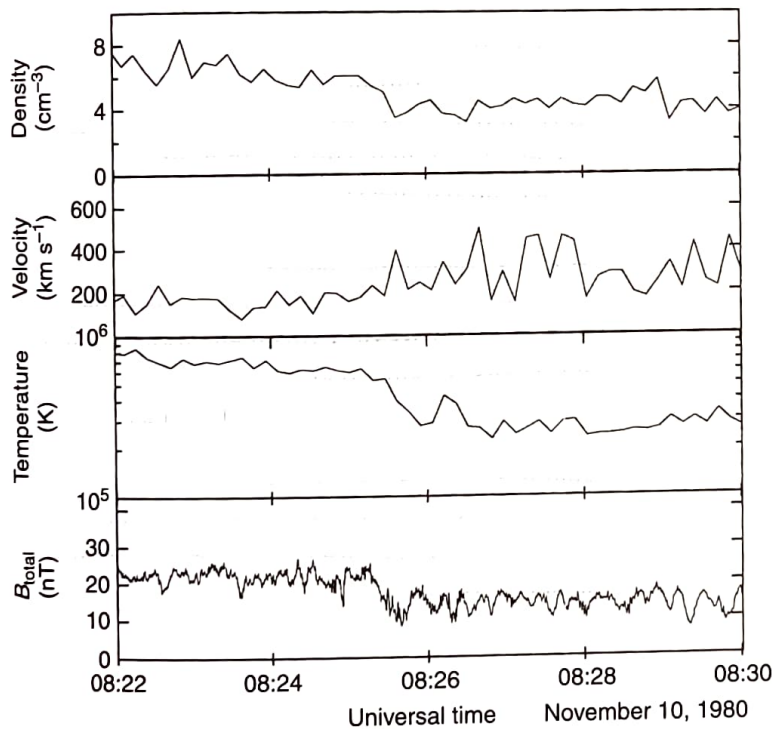


FIGURE 6.8. Electron density, velocity, temperature, and magnetic field strength during the switch-on shock shown in Figure 6.7.

43 times smaller than the ion inertial length. We can only determine the orientation of the normal to the shock to an accuracy of several degrees. Even when we have an accurate average orientation, it will vary

with time as the spacecraft encounters it. Since we expect the “perpendicular” shock to exist only in a range of about 1° about the exactly perpendicular orientation, it will be almost as rare as the nearly

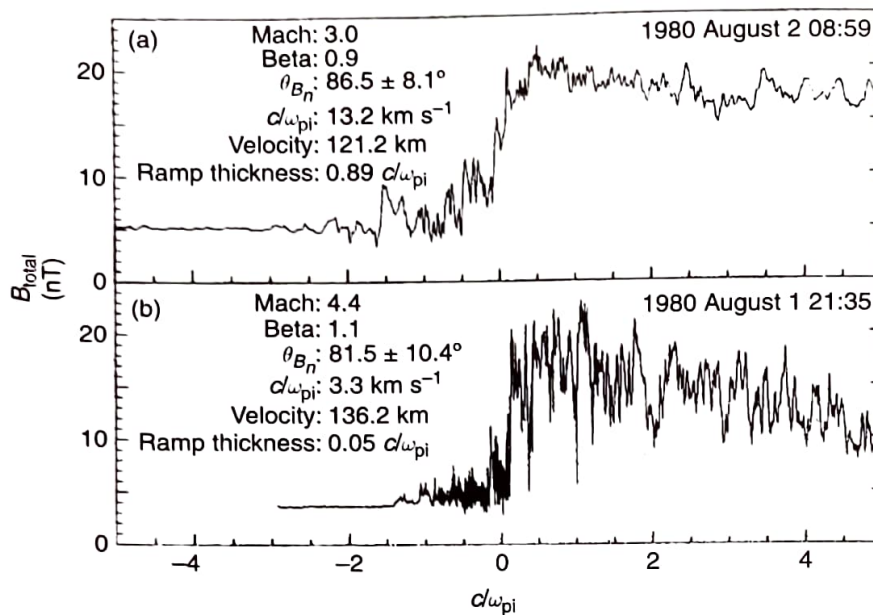


FIGURE 6.9. Magnetic field profile across two supercritical nearly perpendicular shocks. The thickness of the ramp of the shock shown in (a) is close to 1 ion inertial length. The scale length in (b) is about 2 electron inertial lengths, implying that this shock is a perpendicular shock.

exactly

parallel shocks we discussed above. Thus, the best we can do observationally is to determine which shocks are very nearly perpendicular and hope that, during one of these shock encounters, the shock will be sufficiently oriented in the perpendicular direction. Figure 6.9 shows the magnetic field through two nearly perpendicular shocks. The top profile has a ramp thickness of 0.9 ion inertial lengths, while the ramp in the lower panel has a thickness of 2 electron inertial lengths. This is the only example found in an examination of high data rate ISEE 1 and 2 shock crossings (Newbury and Russell, 1996). Thus, while it seems clear that thin, electron-scale shocks can exist, their scarcity results in their existence being principally of academic interest in solar system plasmas.

6.5 OBSERVATIONS UNDER TYPICAL CONDITIONS

The Rankine-Hugoniot relations determine only the jump in parameters across the shock. Although this is very important information, it does not inform us how the dissipation, heating, and thermalization occur. These latter processes make the study of shocks extremely interesting. Figure 6.10 shows three components of the magnetic field across a low Mach number quasi-perpendicular

shock. Clearly, the shock is a source of many different waves. Waves are growing in the shock ramp and damping as they move upstream and downstream. These waves arise because the shock produces "free energy" that can be converted to heating of the plasma by wave generation and the subsequent absorption of that wave. The lowest-frequency upstream wave is clearly propagating along the shock normal direction, \mathbf{n} , as the wave does not have any component in this direction. The upstream high-frequency wave does not appear in the total magnetic field, so it must be propagating along the magnetic field. The downstream high-frequency wave propagates at an angle to the field since it does have a compressional component. Waves can move upstream against the solar-wind flow even though the solar wind is supersonic, because the whistler-mode, or right-handed electromagnetic wave, which oscillates at frequencies greater than the proton gyro-frequency, propagates faster than the solar-wind flow along their wave normal. Moreover, the group velocity, at which the energy of the wave propagates, is faster than the wave phase velocity. Thus, a phase standing structure can form as the low frequency wave in Figure 6.10 and be continually provided with energy from the shock. Thus, the wave maintains a temporally steady profile even while damping as the incoming solar wind flows through it.

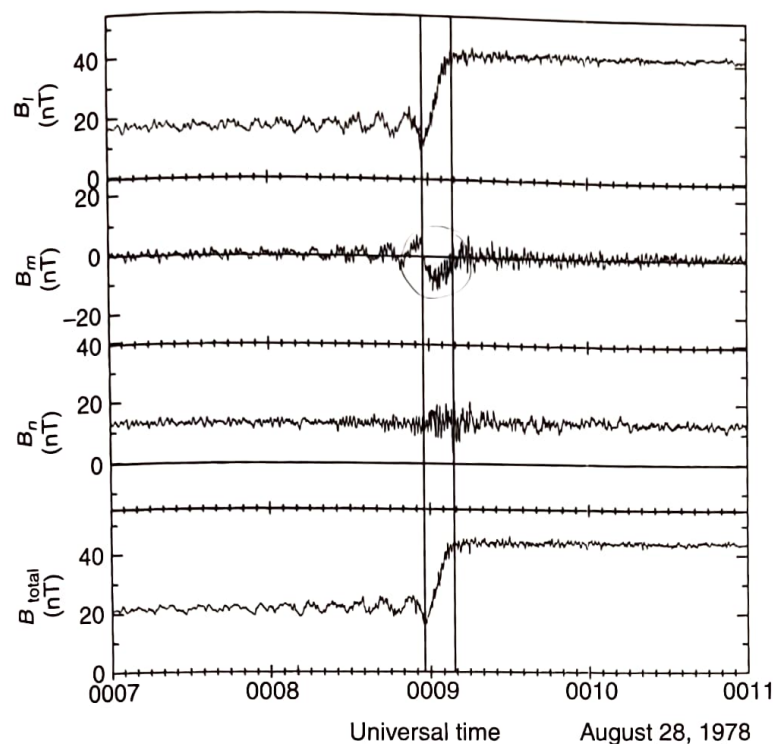


FIGURE 6.10. Magnetic field measurements of a low-beta, subcritical, quasi-perpendicular shock in shock normal coordinates. Except within the shock ramp, the magnetic field is contained within the l - n plane and the shock normal points upstream along the positive n -direction. The two solid lines define the thickness of the shock ramp.

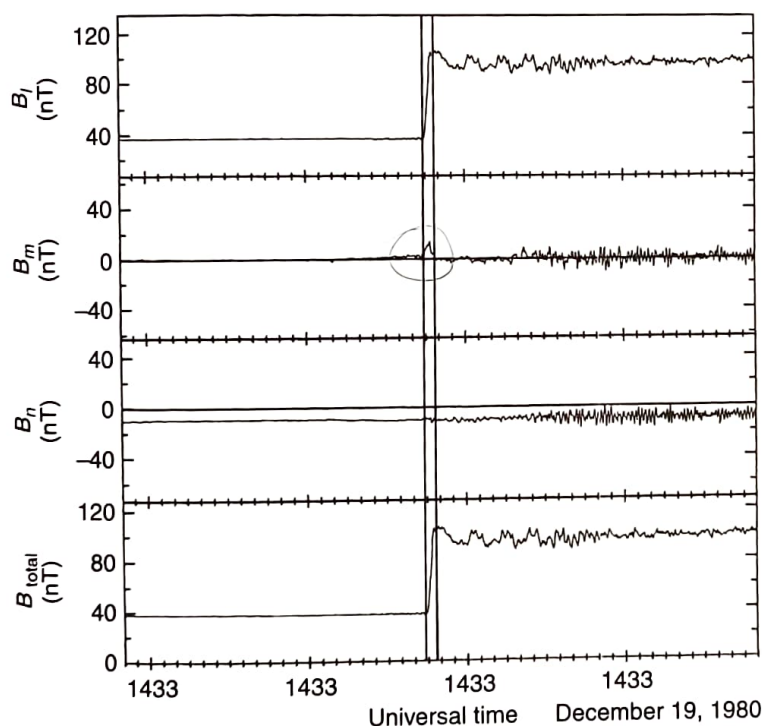


FIGURE 6.11. Magnetic field measurements of a low-beta, marginally critical, quasi-perpendicular shock in shock normal coordinates.

At higher Mach numbers, the waves cannot move upstream and the waves are all carried downstream, as shown in Figure 6.11. Note here the small B_m -component of the field as the shock is

crossed and the slow growth of the high-frequency transverse waves downstream. Here the low-frequency downstream "wave" seen in the total field may not be due to a plasma instability but

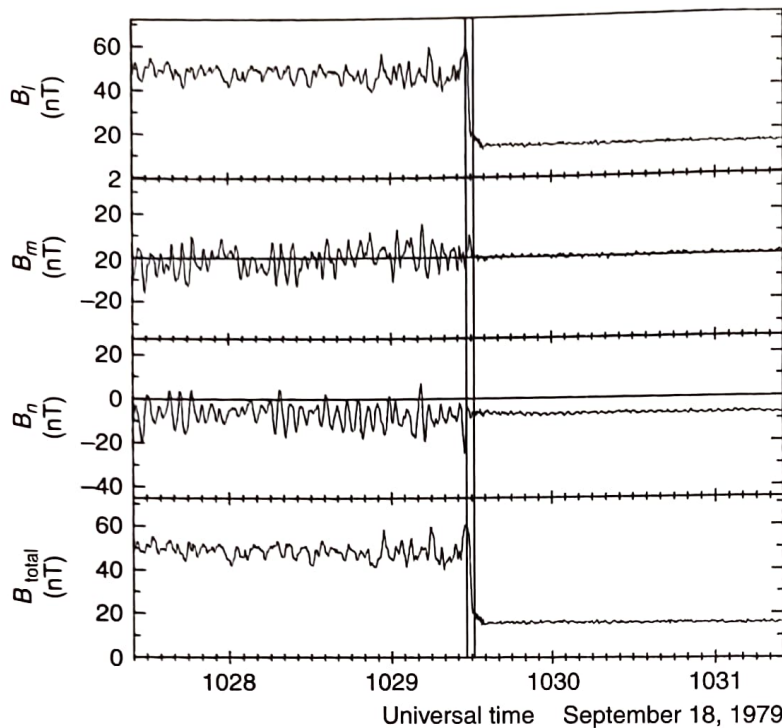


FIGURE 6.12. Magnetic field measurements of a low-beta, supercritical, quasi-perpendicular shock in shock normal coordinates.

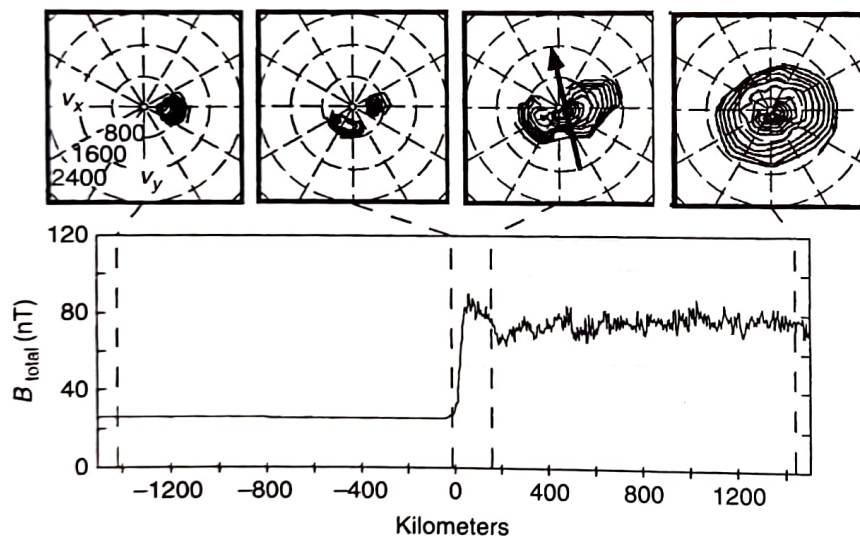


FIGURE 6.13. Magnetic field strength and two-dimensional ion phase space distributions for a low-beta, supercritical, quasi-perpendicular shock. The dashed lines show where the ion measurements were obtained.

rather just due to the bunching of the ion gyration at the thin shock. The thermal spread of the ions allows the ion motion to become less bunched downstream. At even higher Mach numbers, the downstream region is very turbulent, as illustrated in Figure 6.12. The downstream waves serve to thermalize the plasma by growing in a velocity space anisotropy produced as the ions cross the shock. The waves reduce the anisotropy and then in turn damp and heat the plasma.

Figure 6.13 shows two-dimensional examples of ion distribution functions just upstream of the shock. In the first panel, we see only the solar-wind beam. In the second panel, we see both the cold solar-wind beam and reflected ions that did not manage to get through the electric potential and the magnetic ramp of the shock. Panel three shows the downstream ion distribution. The reflected ions have now been swept through the shock and into the magnetosheath. They have been scattered by the

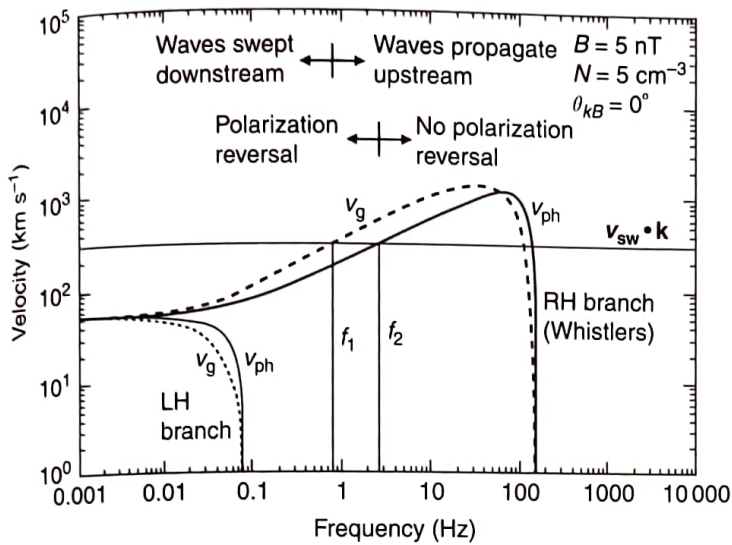


FIGURE 6.14. Phase and group velocities for typical conditions in solar wind near 1 AU, illustrating how whistler-mode waves can group stand (at f_1) or phase stand (at f_2). The velocity of the solar wind along the wave normal, $v_{sw} \cdot k$, will sweep wave energy downstream at frequencies below f_1 and reverse their polarization below f_2 .

waves but still possess a lot of free energy for the production of waves. This free energy continues to produce waves until it is depleted. The waves damp in the plasma and result in the thermalization of the plasma. The fourth panel shows the particle distribution when it has lost most of its velocity space anisotropy and is essentially completely thermalized. The scale downstream over which these waves exist may be very long.

The upstream whistler-mode waves that are propagating at a small angle to the magnetic field are no less interesting than the low-frequency turbulence. Whistler-mode waves are generally associated with electrons which have little mass and therefore momentum, but move quite rapidly for the same energy or temperature. As Figure 6.14 illustrates, the phase and group velocities of whistler-mode waves can exceed the speed of the solar wind along the wave normal for ordinary solar-wind conditions. There is an interesting frequency range for these waves where the group velocity that is faster than the phase velocity can move upstream while the phase velocity is carried downstream. Thus, the wave appears to be left handed when it is actually right handed in the plasma. Moreover, it produces a very interesting power spectrum, as shown in Figure 6.15. If the wave spectrum in the plasma frame were the dark shaded spectrum from 2–5 Hz, and these were the frequencies corresponding to group velocity standing and phase velocity standing waves in the solar-wind flow,

then the waves at 5 Hz would be Doppler shifted to 0 Hz. Lower frequencies can be Doppler shifted to higher frequencies than zero but are polarization reversed. Above 1 Hz in this example, the waves no longer have a group velocity that can transport wave energy upstream, and a sudden drop off of wave energy is seen. The phenomenon reminds us how much Doppler shifting of waves in the solar wind affects their appearance in our sensors. We must always convert the measurements to the plasma frame to understand how these waves are interacting with the plasma constituents.

6.6 THE CRITICAL MACH NUMBER

The concept of a critical Mach number arises from the evolutionary model of shock formation in which the shock is formed from a series of wave packets that overtake one another to form a single steepened wave packet. At low Mach numbers, resistive processes can supply the dissipation required by the Rankine-Hugoniot equations. These resistive processes gradually decouple the magnetic and fluid oscillations, and the phase speed of the steepened wave approaches the sound speed. Thus, if another magnetosonic pulse, which steepens in the same evolutionary manner, is launched and the flow speed is greater than the sound speed, the second pulse will not reach the first pulse. For a proper shock transition,

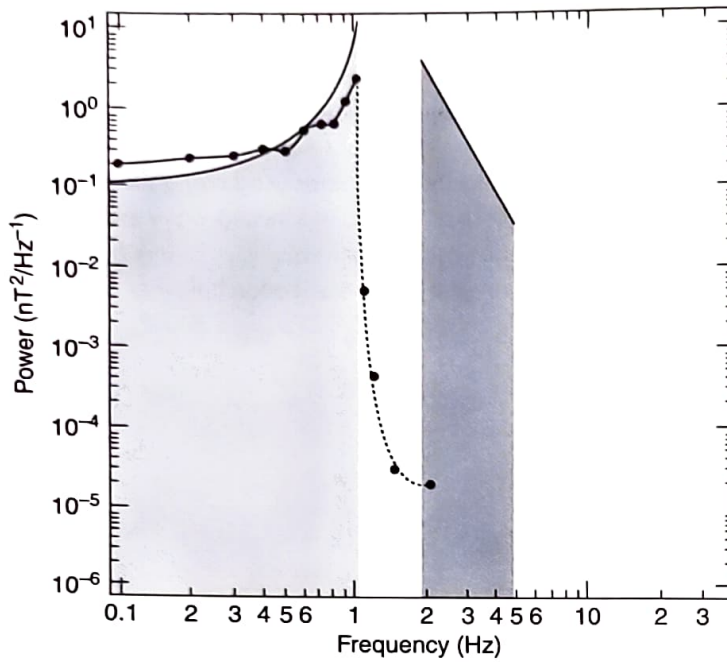


FIGURE 6.15. Illustration of how whistler-mode waves are affected by Doppler shifting by the solar wind. The spectral slice (dark shading) from 2–5 Hz in the solar-wind frame becomes the lower-frequency (light gray) region in the spacecraft frame. The sharp upper-frequency ledge in the spacecraft frame is the sharp lower ledge in the solar-wind frame when the waves are swept downstream at lower frequencies.

dissipation must cause all downstream perturbations to die out away from the shock layer (e.g., Kennel, Edmiston, and Hada, 1985). Thus, the point downstream where the flow speed is equal to the sound speed is the point where resistivity alone cannot provide the required shock dissipation. This is called the critical Mach number. New dissipation mechanisms are required in addition to resistive heating to satisfy properly the predictions made by the Rankine-Hugoniot equations when the upstream Mach number is above this critical Mach number (Kantrowitz and Petschek, 1966; Woods, 1969; Coroniti, 1970). The ratio between the upstream magnetosonic Mach number and the critical Mach number is called the ratio of criticality (M/M_c). When the Mach number is below the critical Mach number, the shock is called “subcritical,” and when it is above, it is called “supercritical.” One of the phenomena that changes with the ratio of criticality is the size of the overshoot, a rise in the magnetic field strength with a thickness of about an ion gyro-radius immediately downstream of the shock ramp. This behavior is illustrated in Figure 6.16.

As stated above, the critical Mach number is the upstream Mach number for which the downstream flow velocity along the shock normal is equal to the downstream gas-dynamic sound speed, for a

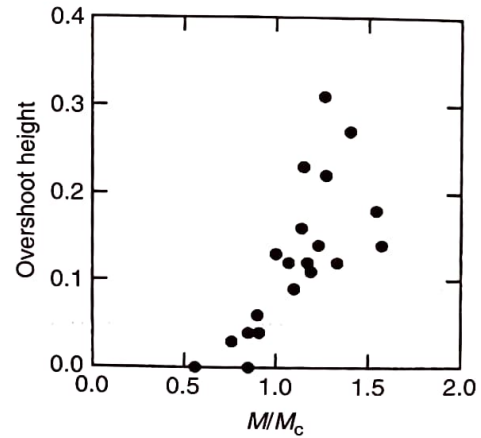


FIGURE 6.16. Overshoot height versus the ratio of the Mach number to the critical Mach number.

particular plasma beta, magnetic field orientation, and ratio of specific heats. Since we have solutions for these two characteristic velocities (see Eqs. (6.17) and (6.21)), we can set them equal to one another and solve for the criterion defining the critical Mach number, recalling that the downstream sound velocity is $(\gamma KT^2/m)^{1/2}$

$$\gamma(a + 0.5c(1 - \delta) + 1 - \gamma) - \gamma^2 = 0. \quad (6.27)$$

The upstream magnetosonic Mach number which satisfies this relation is the critical Mach

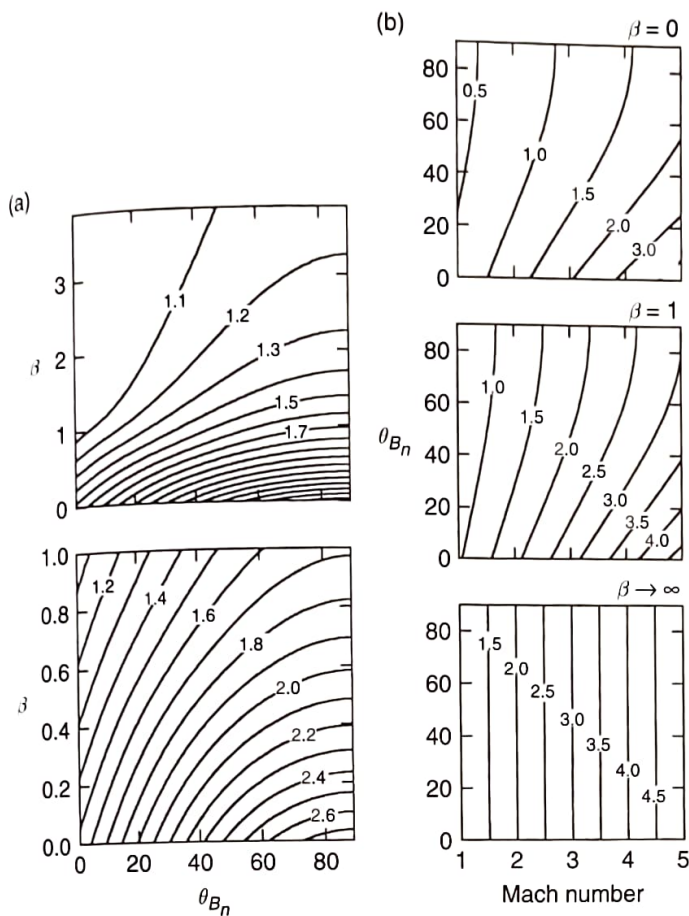


FIGURE 6.17. Contours of (a) the critical Mach number versus beta and θ_{Bn} and (b) the ratio of criticality versus θ_{Bn} and Mach number for $\beta = 0$, $\beta = 1$, and $\beta \rightarrow \infty$. The lower left panel in (a) is an expansion of the low-beta portion of the upper left panel in (a) to display more clearly the θ_{Bn} dependence in this region.

number. It is interesting to see how the critical Mach number varies with plasma beta and θ_{Bn} for a ratio of specific heats of 5/3. Figure 6.17 shows contours of the critical Mach number for varying betas and magnetic field orientations as well as the ratio of criticality versus θ_{Bn} and Mach number for various plasma betas. The critical Mach number is lowest for parallel shocks and increases monotonically as the shock becomes more perpendicular. It drops with increasing beta. The ratio of criticality, in turn, increases monotonically with upstream Mach number and drops somewhat with increasing θ_{Bn} . At high beta, there is very little θ_{Bn} dependence.

6.7 SHOCK DISSIPATION

Ideally, the collisionless shock develops a thin layer in which there is an electric potential drop

with an electric field pointing in the direction of the incoming flow so that positive ions are decelerated. In addition, the magnetic field rise results in the deflection of some particles with large pitch angles, even without the deceleration by the electric field. What happens to the reflected particles depends on the direction of the magnetic field relative to the shock normal. In the frame of reference of the solar wind, the reflected ion has a velocity of twice the solar-wind velocity because the particle is now moving backward at its previous forward velocity. However, the upstream magnetic field is acting on this backward-moving particle and turns its motion around. The ion can only move a finite distance upstream until it is turned around and moves downstream through the shocks, unless the upstream field is at an angle of less than 39° to the shock normal. Then, the upstream reflection velocity is too high to be turned around by the gyro-motion to

39°

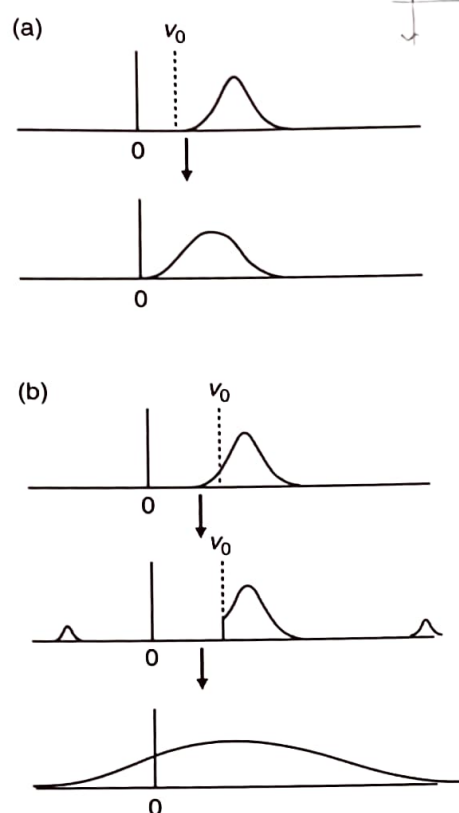


FIGURE 6.18. Variation of shock dissipation with Mach number. (a) The solar wind approaches a weak shock with a low electric potential drop so that the entire ion distribution can pass through without reflection. (b) A strong shock has a potential drop that turns around part of the distribution so that it returns to the solar wind only to gyrate around the magnetic field and cross the shock at higher speed. The downstream ions are heated in crossing the shock and thermalized with increasing distance downstream.

cross the shock. At angles less than 39° , ions move upstream upon reflection. In practice, this process is very non-time-stationary. Moreover, hot ions created downstream can also move upstream, especially for supercritical shocks. In either case, the result is that ion beams can move upstream. We can simulate this process with hybrid codes, following only ion motion, or with fully kinetic codes. For ions at shocks with radii of curvature of the terrestrial planets, the radius of curvature is an important factor in determining the properties of the foreshock. These simulations will be discussed in Chapter 7.

We discuss the foreshock in the following two sections, but first let us examine how upstream reflection and subsequent drift back across the shock lead to dissipation.

Figure 6.18 presents a simplistic explanation of how ion reflection can lead to the expected dissipation in the plasma downstream of the shock. In Figure 6.18(a) we show a low Mach number shock in which the energy of the incoming flow is high enough and the thermal spread low enough such that the whole distribution passes through the electric potential drop of the shock and no particles are reflected. The downstream distribution function is heated and slowed by the compression, and the waves present are sufficient to produce the conditions required by the Rankine-Hugoniot equations. In Figure 6.18(b), we show a high Mach number shock with a larger potential barrier that reflects some of the ions back into the solar wind. In a quasi-perpendicular shock (in which the angle between the upstream magnetic field and the shock normal is greater than 39°), these ions turn around and drift back into the shock and enter the magnetosheath, where they are eventually thermalized, as illustrated in Figure 6.18(b).

One might expect that the electric potential that slows the ions would accelerate the electrons an equivalent amount, but electrons receive little heating at the shock. The reason that electrons can avoid being accelerated is tied to the magnetic structure of the shock, at least at low Mach numbers where the heating paradox occurs. Due to their small gyro-radii, electrons follow the magnetic field as shown in Figure 6.19, whereas ions move straight across the shock parallel to the normal. The magnetic field rotates as it crosses the shock in just the direction to move the electrons across solar-wind equipotentials to compensate for much of the electric potential drop across the shock normal (Goodrich and Scudder, 1984). This phenomenon is caused by the difference in the masses of electrons and ions. As a result, the electrons, which are generally warmer than ions in the solar wind, are the cooler species by about a factor of seven in the magnetosheath and the plasma sheet after they enter the Earth's tail.

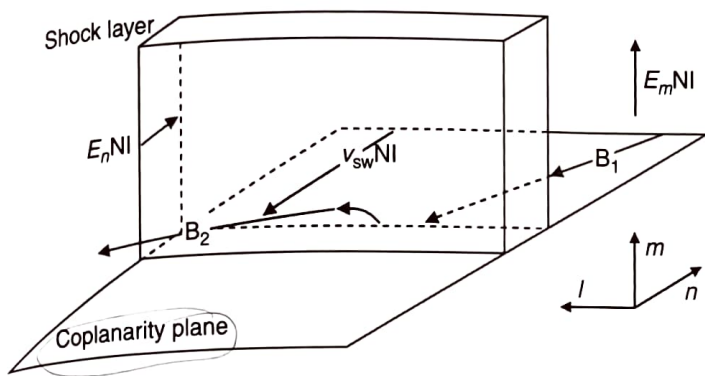


FIGURE 6.19. Schematic of how the electrons move along the magnetic field and are able to avoid the full effect of the potential drop across the shock by moving across interplanetary electric potentials. Quantities labeled "NI" are in the normal incidence frame where the solar-wind velocity is along the shock normal.

6.8 QUASI-PARALLEL SHOCK AND ION FORESHOCK

As mentioned above, the reflected ions can move upstream when the magnetic field makes an angle of less than 39° to the shock normal. Moreover, downstream particles can also cross the shock and move upstream. Ions moving upstream have to pass through the incoming solar wind and thus produce various ion instabilities in which waves grow from the free energy in the beam. These waves can be right handed when the unstable wave is moving slower than the particle and left handed when the particle and wave interact head on. As a result, the region upstream of the quasi-parallel shock, known as the foreshock, is a regular showcase of wave phenomena. Figure 6.20 shows examples of waves seen in this region.

In general, the waves are being carried backward by the solar wind into the shock and are adding to the dissipation. Moreover, they propagate and steepen while they simultaneously alter the particle distributions that produce them. This steepening is illustrated in Figure 6.21. This close coupling and mutual interaction make it difficult to sort out cause and effect, and this underlines the need to use both observation and numerical simulation to determine the physics of these shocks.

A very interesting phenomenon occurs when these waves reach the location of the quasi-parallel shock. The waves suddenly grow and the shock reforms. This process is illustrated in Figure 6.22.

6.9 THE ELECTRON FORESHOCK

Electrons are accelerated back into the solar wind at a much higher velocity and therefore have a foreshock boundary much closer to the tangent field line. They can be accelerated right up to the tangent point, albeit with infinitesimal flux (see Figure 6.23). This beam produces Langmuir oscillations at the plasma frequency of the solar wind.

It is instructive to review briefly the reflection of the electrons, often called fast-Fermi acceleration, to gain insight into the nature of this electron beam. Figure 6.24(a) shows the electron angular distribution in the de Hoffman-Teller frame, in which the solar-wind flow is parallel to the magnetic field. The closer the magnetic field is to being tangent to the shock normal, the higher the transformation velocity is, so that the center of the electron distribution moves upward in this diagram. The curved dashed lines indicate that part of the distribution that cannot cross the shock because of the combined action of the magnetic and electric fields. As the de Hoffman-Teller velocity becomes faster and faster, the reflected portion of the distribution moves to higher and higher energy, and the flux reflected becomes less and less. This is made more quantitative in Figure 6.24(b). The result is a Langmuir wave generation region whose extent is controlled by the curvature of the shock. This has relevance to both planetary and interplanetary shocks.

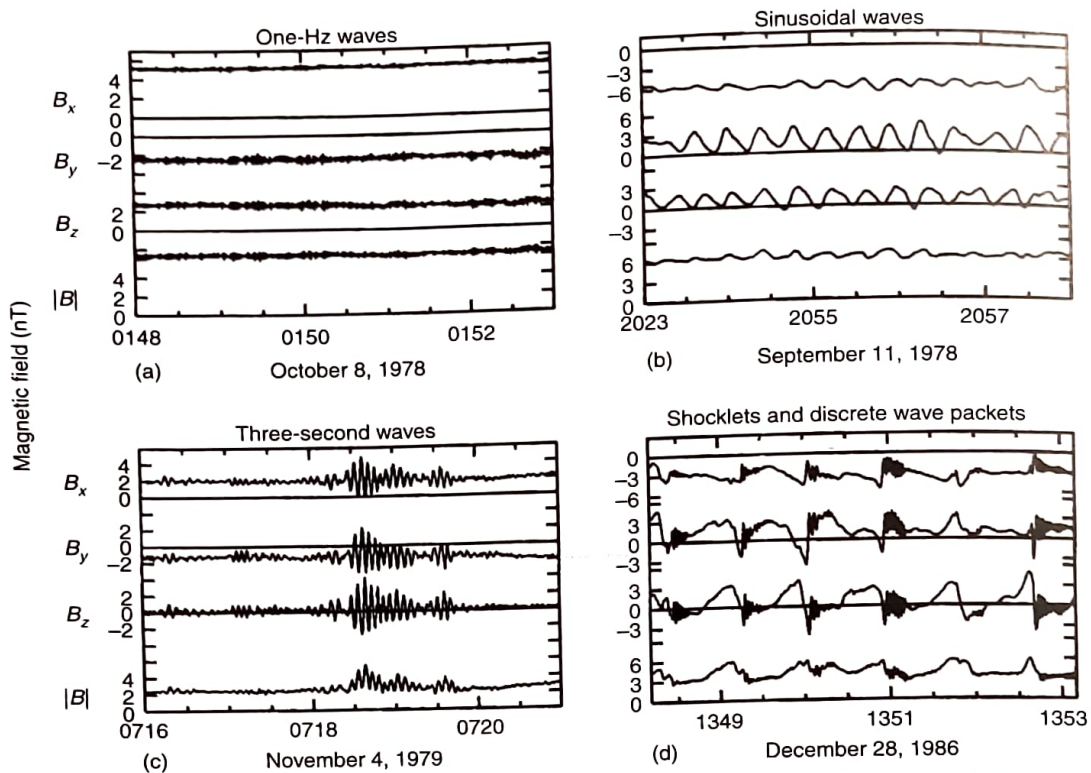


FIGURE 6.20. Examples of upstream waves observed by the ISEE 1 and 2 spacecraft. Magnetic field data are in the geocentric solar ecliptic coordinate system with x to the Sun and z along ecliptic north. (a) Waves commonly called "one-Hz" waves. (c) Three-second waves, whose strength is so large they change the magnitude of the field. Sinusoidal waves (b) are thought to steepen (d), producing shocklets and whistler-mode wave packets.

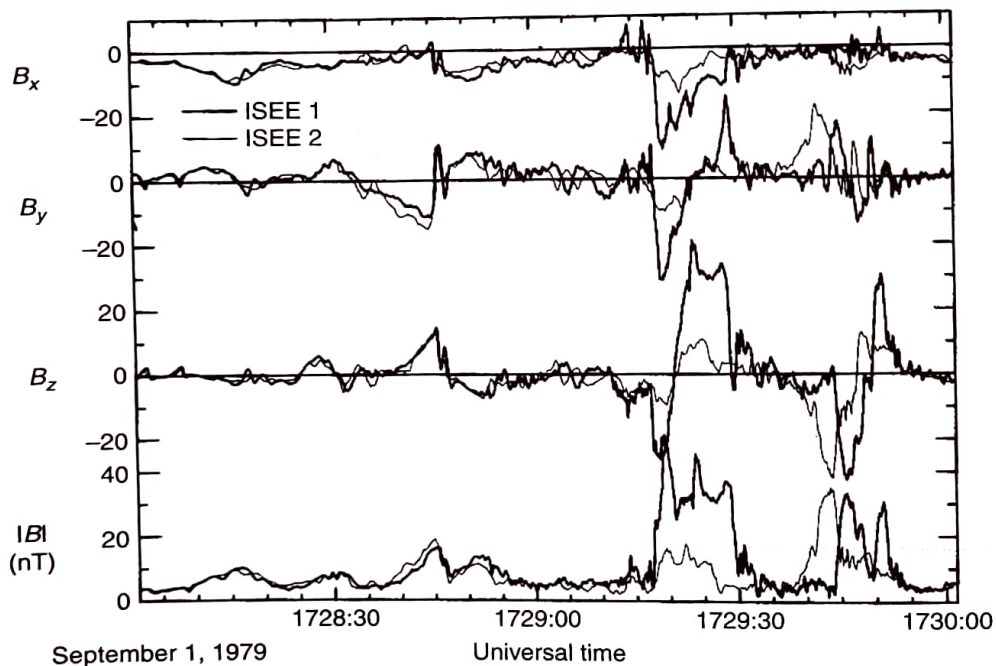


FIGURE 6.21. Shock reformation observed in measurements of the magnetic field by the ISEE 1 and 2 spacecraft as they near the bow shock from the upstream side, with ISEE 2 further upstream than ISEE 1 (heavy line). As the ISEE 1 approaches the shock, the upstream waves both see an increase in strength to shock-like amplitudes.

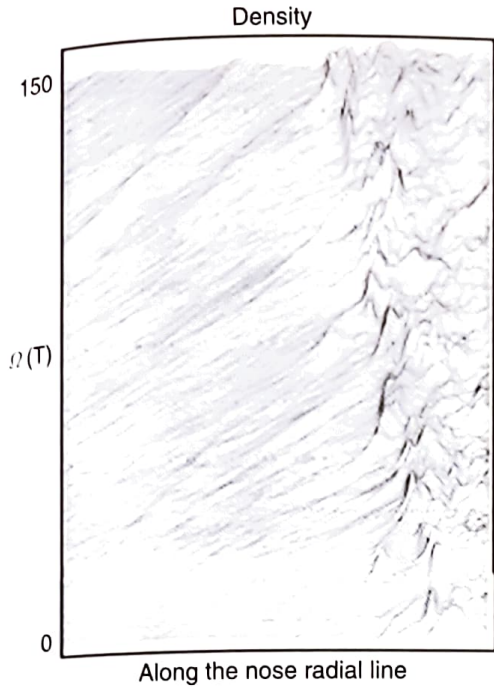


FIGURE 6.22. Two-dimensional hybrid simulation showing upstream waves in the solar-wind density being convected into the shock on the right. As the waves approach the average location of the shock, they strengthen and become part of the shock. (From N. Omid, with permission; private communication, 2015.)

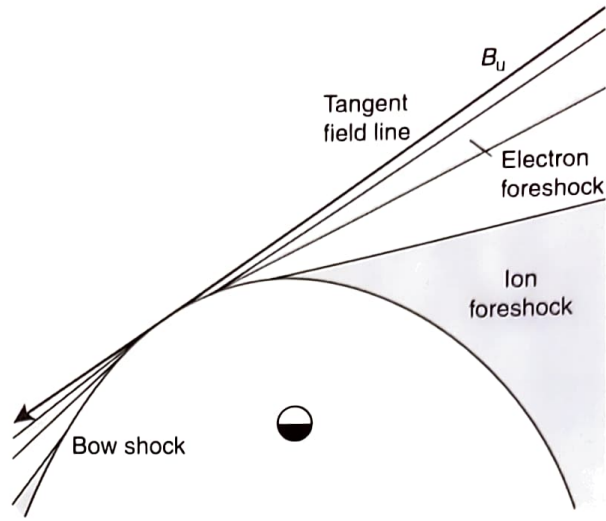


FIGURE 6.23. Schematic of the location of the electron and ion foreshocks in relationship to the magnetic field line that is tangent to the bow shock.

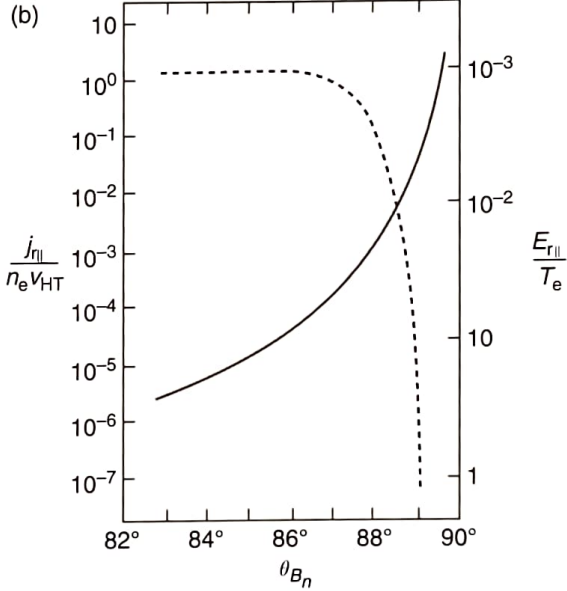
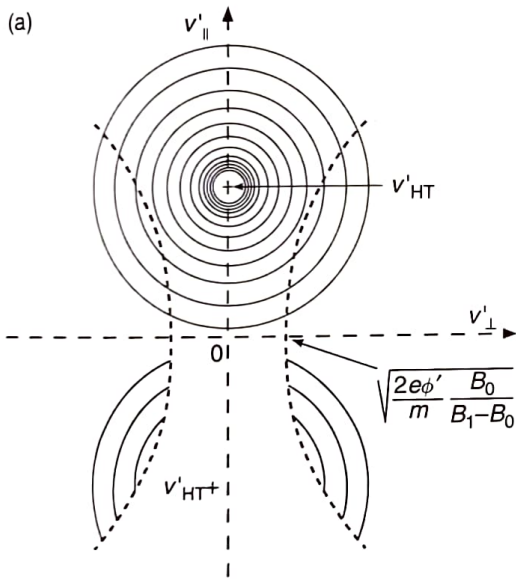


FIGURE 6.24. Schematic of the production of an electron beam at the bow shock by the fast-Fermi acceleration mechanism, shown in the de Hoffman–Teller reference frame. The curved dashed lines in (a) indicate that portion of the electron distribution that cannot pass through the ramp because of the magnetic mirror effect countering the potential drop. The closer the magnetic field line is to tangency, the further is the distribution above the axis, and the smaller is the portion of the distribution reflected, the higher the energy of the reflected ions. B_0 and B_1 are upstream and downstream magnetic fields; v'_{HT} is the de Hoffmann–Teller speed; ϕ' is the shock potential; n_e and T_e are the upstream electron density and temperature; $j_{||}$ and $E_{r||}$ are the flux and energy per charge of the reflected beam along the magnetic field; and θ_{B_n} is the shock normal angle. (After Leroy and Mangeney, 1984.)

6.10 SUMMARY

The Rankine–Hugoniot equations were derived from the MHD formalism using the normal incidence frame, in which the flow is along the shock normal. Scalar quantities such as densities, temperatures, and magnetic field strengths are not frame dependent and can be directly compared. However, we remind the reader that there may be a component of velocity in the measurement frame that is orthogonal to the normal. Therefore, in practice, care must be exercised in comparing measured and predicted velocities. We also remind the reader that the thickness of the bow shock is of the order of the ion inertial length, and at times of the order of the electron inertia length. Thus the dissipative processes in the shock must be treated at the kinetic scale. MHD at best only describes how much dissipation is required at the shock, not how it occurs.

This chapter provides only a cursory review of the physics of collisionless shocks. Much has been omitted, especially in the area of high Mach number shocks where the magnetic field becomes turbulent and large overshoots appear in the magnetic field just downstream from the shock. The bow shocks of the outer planets are particularly strong and exhibit significant overshoots. We have given wave steepening in the upstream region short shrift and not discussed shocklets and discrete wave pockets (whistlers) that arise when the waves have room to evolve before they are swept into the magnetosheath. We have not addressed many of the waves generated at the shock and propagating into the solar wind. Some of these form standing waves that may be considered to be part of the shock structure. We have also concentrated solely on shocks associated with the fast mode. We have not discussed the boundaries of the foreshock, and we have not discussed a very interesting wave that is generated at the bow shock and convected downstream, the mirror-mode wave that appears to damp only over very long time scales.

Much of our understanding of the collisionless shock arises from the observations, modeling, and theory of bow shocks, but shocks also occur in the solar wind in front of ICMEs and where fast

streams overtake slower streams. Since the velocity of the magnetosonic fast mode decreases as the solar wind moves away from the Sun, an initially linear wave can become non-linear when its speed exceeds that of the magnetosonic fast mode. When observed, the steepening process resembles that of a tidal bore in which small waves overtake other waves and make a stronger, single wave.

Shocks can accelerate particles in many ways. Particles can drift along the shock front in the direction of the electric field and pick up energy from the difference in electric potential. They can also be reflected by a moving shock front, resulting in what is called Fermi acceleration. If a particle is caught between two shocks, or even two waves approaching each other, the particle accelerates as work is done on them by the approaching shocks, like a table tennis ball between a descending paddle and the table. This is called second-order Fermi acceleration.

Collisionless shocks are important for many reasons, not only in their role in the energization of charged particles, but also because of their effect on the bulk properties of the flow. They are important intellectually as they are a point of common interest for astrophysicists, plasma physicists, and space physicists. They also show the importance of a strong link between observation and simulation in understanding space physics phenomena in detail.

Additional reading

- FARRIS, M. H., C. T. RUSSELL, R. J. FITZENREITER, and K. W. OGILVIE (1994). The subcritical, quasi-parallel, switch-on shock. *Geophys. Res. Lett.*, 21, 837–840. Treatment of an unusual form of collisionless shock.
- RUSSELL, C. T., ed. (1988). Multipoint magnetospheric measurements. *Adv. Space Res.*, 8(9). Oxford: Pergamon Press, 464 pp. Collection of research papers on multipoint measurements, many of them on the bow shock and the magnetosheath.
- RUSSELL, C. T., ed. (1994). The magnetosheath. *Adv. Space Res.*, 14. Oxford: Pergamon Press, 135 pp. Collection of research papers on the magnetosheath during the height of collisionless shock research.